

# Using open data to rapidly benchmark biomolecular simulations: Phospholipid conformational dynamics

Hanne S. Antila,<sup>\*,†</sup> Tiago M. Ferreira,<sup>‡</sup> O. H. Samuli Ollila,<sup>¶</sup> and Markus S. Miettinen<sup>\*,†</sup>

<sup>†</sup>*Department of Theory and Bio-Systems, Max Planck Institute of Colloids and Interfaces, 14424 Potsdam, Germany*

<sup>‡</sup>*NMR Group — Institute for Physics, Martin-Luther University Halle-Wittenberg, 06120 Halle (Saale), Germany*

<sup>¶</sup>*Institute of Biotechnology, University of Helsinki, 00014 Helsinki, Finland*

E-mail: hanne.antila@mpikg.mpg.de; markus.miettinen@iki.fi

## Abstract

Molecular dynamics (MD) simulations are widely used to study the atomistic structure and dynamics of biomembranes. It remains unknown, however, how well the conformational dynamics observed in MD simulations correspond to those occurring in real life phospholipids. The accuracy of such time scales in MD can be assessed by comparing against the effective correlation times  $\tau_e$  of the C-H bonds measured in nuclear magnetic resonance experiments (J. Chem. Phys. 142 044905 (2015)).

Here, we use a large set of open data trajectories made public by the NMRlipids project ([nmrlipids.blogspot.fi](http://nmrlipids.blogspot.fi)) to perform an unprecedented test on the conformational dynamics of phospholipids as produced by several commonly used MD models (force fields). We find that none of the tested force fields to reproduce all the effective correlation times within experimental error, much like they do not provide accurate conformational ensembles (J. Phys. Chem. B 119 15075 (2015)). However, the dynamics observed in CHARMM36 and Slipids were more realistic than those seen in the Amber Lipid14, OPLS-based MacRog, and GROMOS-based Berger force fields, where

dynamics of the glycerol backbone was unrealistically slow. **1.Tiago: We need a punchline highlighting that the results and findings obtained are extremely important for the lipid MD simulation community and that they were only possible due to the open data**

## 1 Introduction

Ever since the conception of Protein Data Bank (PDB)<sup>1,2</sup> and GenBank,<sup>3,4</sup> open access to standardised and searchable pools of experimental data has revolutionized scientific research. Constantly growing and improving in fidelity due to collaborative effort,<sup>5–8</sup> the now hundreds of databanks<sup>9</sup> fuel the data-driven development of biomolecular structure determination,<sup>10</sup> refinement,<sup>11</sup> prediction,<sup>12</sup> and design<sup>13</sup> approaches, as well as development of drugs,<sup>14,15</sup> materials,<sup>16,17</sup> and more.<sup>18,19</sup> It is clear that open data enables scientific progress that is far beyond the resources of a single research group or institute. Consequently, the call for public availability and conservation of data has extended to molecular dynamics (MD) simulation trajectories of biomolecules,<sup>20–22</sup> and the discussion on how and by whom such databanks for dynamic structures would be set up is currently active.<sup>23–26</sup> While no general MD tra-

jectory databank currently operates, individual databanks are accepting contributions on nucleic acid,<sup>27</sup> protein/DNA/RNA,<sup>28</sup> cyclodextrin,<sup>29</sup> G-protein-coupled receptor,<sup>30</sup> and lipid bilayer<sup>31</sup> simulations.

Since 2013, the NRMlipids Project ([nmrlipids.blogspot.fi](http://nmrlipids.blogspot.fi)) has promoted a fully open collaboration approach, where the whole scientific research process—from initial ideas and discussions to analysis methods, data, and publications—is all the time publicly available.<sup>32</sup> While its main focus has been on conformational ensembles of different lipid headgroups and on ion binding to lipid membranes,<sup>32–34</sup> the NRMlipids Project has also built a databank<sup>31</sup> ([zenodo.org/communities/nmrlipids](http://zenodo.org/communities/nmrlipids)) containing hundreds of atomistic MD trajectories of lipid bilayers and indexed at [nmrlipids.fi](http://nmrlipids.fi).

MD databanks are expected to be particularly relevant for disordered biomolecules, such as biological lipids composing cellular membranes or intrinsically disordered proteins. These, in contrast to folded proteins or DNA strands, cannot be meaningfully described by the coordinates of a single structure alone. Realistic MD simulations, however, can provide the complete conformational ensemble and dynamics of such molecules, as well as enable studies of their biological functions in complex biomolecular assemblies. Unfortunately, the current MD force fields largely fail to capture the conformational ensembles of lipid headgroups and disordered proteins.<sup>32,34–37</sup> Therefore, before they can be used to draw conclusions, the quality of MD simulations must always be carefully assessed against structurally sensitive experiments. For lipid bilayers, such evaluation is possible against NMR and scattering data.<sup>38</sup>

Here, we demonstrate the use of a pre-existing, publicly available set of MD trajectories to rapidly evaluate the fidelity of phospholipid conformational dynamics in state-of-the-art force fields. The speed at which individual molecules sample their conformational ensemble is traditionally used to assess if a given MD simulation has converged. Going beyond such practicalities, realistic dynamics are particularly desired for the intuitive interpretation

of NMR experiments sensitive to molecular motions,<sup>39</sup> as well as to understand the dynamics of biological processes where molecular deformations play a rate-limiting role, such as membrane fusion.<sup>40</sup> The here presented comprehensive comparison of dynamics between experiments and different MD models at various biologically relevant compositions and conditions is thus likely to facilitate the development of increasingly realistic phospholipid force fields.

Above all, our results demonstrate the power of publicly available MD trajectories in creating new knowledge at a lowered computational cost and high potential for automation. We believe that this paves the way for novel applications of MD trajectory databanks, as well as underlines their usefulness—not only for lipid membranes, but for all biomolecular systems.

## 2 Methods

### Lipid conformational dynamics in NMR data.

We analyzed the veracity of phosphatidylcholine (PC) lipid dynamics in MD based on two quantities that are readily available from published<sup>39,41–43</sup> <sup>13</sup>C-NMR experiments and directly quantifiable from atomistic MD simulations: The effective C–H bond correlation times  $\tau_e$ , and the spin-lattice relaxation rates  $R_1$ .

#### Effective C–H bond correlation times $\tau_e$ .

In a lipid bilayer in liquid crystalline state, each individual lipid samples its internal conformational ensemble and rotates around the membrane normal. Lipid conformational dynamics are reflected in the second order autocorrelation functions of its C–H bonds

$$g(\tau) = \langle P_2(\vec{\mu}(t) \cdot \vec{\mu}(t + \tau)) \rangle, \quad (1)$$

where the angular brackets depict time average,  $\vec{\mu}(t)$  is the unit vector in the direction of the C–H bond at time  $t$ , and  $P_2$  is the second order Legendre polynomial  $P_2(x) = \frac{1}{2}(3x^2 - 1)$ . To analyze the internal dynamics of lipids, the C–H bond autocorrelation function is often written

as a product

$$g(\tau) = g_f(\tau)g_s(\tau), \quad (2)$$

where  $g_f(\tau)$  characterizes the fast decays owing to, e.g., the internal dynamics and rotation around membrane normal, and  $g_s(\tau)$  the slow decays that originate from, e.g., lipid diffusion between lamellae with different orientations and periodic motions due to magic angle spinning conditions (Fig. 1). Ferreira et al.<sup>41</sup> have experimentally demonstrated that for all phospholipid carbons the motional correlation times contributing to  $g_f$  are well below  $\mu\text{s}$ , and to  $g_s$  well above  $100 \mu\text{s}$ . This separation of time scales gives rise to the plateau  $g(1 \mu\text{s} \lesssim \tau \lesssim 100 \mu\text{s}) = S_{\text{CH}}^2$  illustrated in Fig. 1.  $S_{\text{CH}}$  is the C-H bond order parameter

$$S_{\text{CH}} = \frac{1}{2} \langle 3 \cos^2 \theta(t) - 1 \rangle, \quad (3)$$

where  $\theta(t)$  is the angle between the C-H bond and the bilayer normal.  $S_{\text{CH}}$  can be independently measured using dipolar coupling in  $^{13}\text{C}$  or quadrupolar coupling in  $^2\text{H}$ -NMR experiments. Knowing the set of  $S_{\text{CH}}$  for all the C-H bonds in a lipid is highly useful in order to evaluate its conformational ensemble.<sup>38</sup>

As  $S_{\text{CH}}$  describe the conformational ensemble of the lipid, the fast-decaying component  $g_f$  of the C-H bond autocorrelation function intuitively reflects the time needed to sample these conformations. The complex internal dynamics containing multiple timescales can be conveniently summarized using the effective correlation time

$$\tau_e = \int_0^\infty \frac{g_f(\tau) - S_{\text{CH}}^2}{1 - S_{\text{CH}}^2} d\tau, \quad (4)$$

which is related to the gray-shaded area below the correlation function in Fig. 1. The  $\tau_e$  detect essentially an average over all the time scales relevant for the lipid conformational dynamics. Their relation to process speeds is intuitive: Increase of long-lived correlations increases  $\tau_e$ .

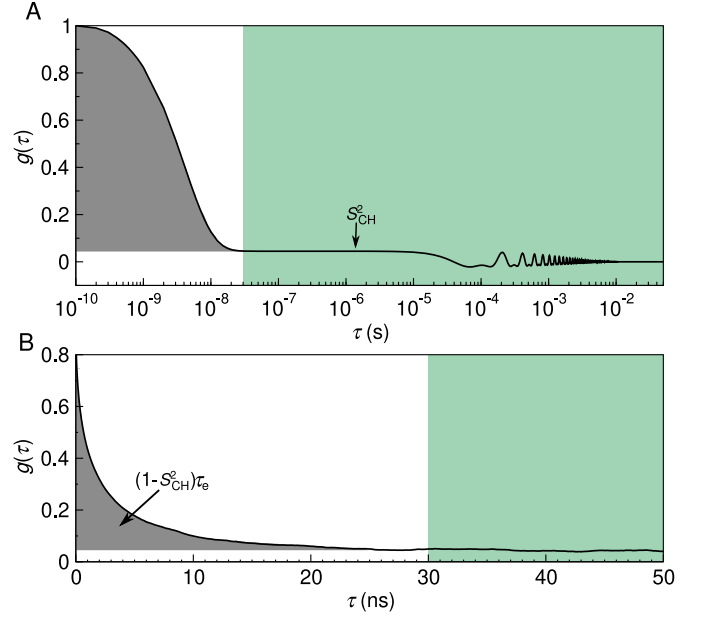


Figure 1: C-H bond autocorrelation function  $g(\tau)$ . (A) Idealised illustration of the fast (white background) and the slow (green) mode of the correlation function. The fast mode decays to a plateau on which  $g(\tau) = S_{\text{CH}}^2$ , while the slow mode gives the final descent to zero. Oscillations at the slow mode region are due to magic angle spinning. (B) Typical  $g(\tau)$  obtained from an MD simulation, showing the decay towards  $S_{\text{CH}}^2$ . The gray area under the curve is equal to  $(1 - S_{\text{CH}}^2)\tau_e$ .

### Spin-lattice relaxation rates $R_1$ .

The C-H bond dynamics relate to  $R_1$ , the spin-lattice relaxation rate, through

$$R_1 = \frac{d_{\text{CH}}^2 N_{\text{H}}}{20} [j(\omega_{\text{H}} - \omega_{\text{C}}) + 3j(\omega_{\text{C}}) + 6j(\omega_{\text{H}} + \omega_{\text{C}})], \quad (5)$$

where  $\omega_{\text{H}}$  is the  $^1\text{H}$  and  $\omega_{\text{C}}$  the  $^{13}\text{C}$ -NMR Larmor frequency, and  $N_{\text{H}}$  the number of hydrogens covalently bonded to the carbon. The rigid dipolar coupling constant  $d_{\text{CH}} \approx -2\pi \times 22 \text{ kHz}$  for the methylene bond. The spectral density  $j(\omega)$  is given by the Fourier transformation

$$j(\omega) = 2 \int_0^\infty \cos(\omega\tau) g(\tau) d\tau \quad (6)$$

of the C-H bond autocorrelation function  $g(\tau)$  (Eq. (1)). Clearly the connection between

$R_1$  and molecular dynamics is not straightforward; the magnitude of  $R_1$  does, however, reflect the relative significance of processes with timescales near the inverse of  $\omega_H$  and  $\omega_C$ . These two frequencies depend on the field strength used in the NMR experiments: Typically  $R_1$  is most sensitive to motions with time scales  $\sim 0.1$ – $10$  ns. (In our experimental data<sup>39,41–43</sup>  $\omega_C = 125$  MHz and  $\omega_H = 500$  MHz, which gives  $(2\pi \times 125 \text{ MHz})^{-1} = 1.3$  ns and  $(2\pi \times 625 \text{ MHz})^{-1} = 0.25$  ns.) A change in  $R_1$ , therefore, indicates a change in the relative amount of processes occurring in a window around the sensitive timescale, but does not give information on the direction (speedup/slowdown) to which the processes changed.

## Data acquisition and analysis.

All the experimental quantities used in this work were collected from the literature sources<sup>39,41–43</sup> cited at the respective figures.

The simulation trajectories were collected from the general-purpose open-access repository Zenodo ([zenodo.org](https://zenodo.org)), with the majority of the data originating from the NMR-lipids Project<sup>32,33</sup> ([nmrlipids.blogspot.fi](https://nmrlipids.blogspot.fi)). The trajectories were chosen by hand based on how well the simulation conditions matched the available experimental data (lipid type, temperature, cholesterol content, hydration), and how precisely one could extract the quantities of interest from the trajectory (length of simulation, system size). Table 1 lists the chosen trajectories of pure POPC (1-palmitoyl-2-oleoyl-glycero-3-phosphocholine) bilayers at/near room temperature and at full hydration; Table 2 lists the trajectories with cholesterol; and Table 3 those with varying hydration. Full computational details for each simulation are available at the cited Zenodo entry.

The trajectories were analyzed using in-house scripts. These are available on GitHub ([github.com/hsantila/Corrtimes/tree/master/teff\\_analysis](https://github.com/hsantila/Corrtimes/tree/master/teff_analysis)), along with a Python notebook outlining an example analysis run. To enable automated analysis of several force fields with differing atom naming conventions, we used the mapping scheme developed within

Table 1: Analyzed open-access MD trajectories of pure POPC lipid bilayers at full hydration. Note that the temperature varied across these openly available simulation data, but in no case was  $T$  lower than in the experiment. Thus, as dynamics slows down when temperature drops, any overestimation of  $\tau_e$  by MD (as typically seen in Fig. 2) would get worse if the simulations were done at the experimental 298 K.

force field	$N_l^a$	$N_w^b$	$T^c$ (K)	$t_{\text{anal}}^d$ (ns)	files <sup>e</sup>
Berger-POPC-07 <sup>44</sup>	256	10240	300	300	[45]
CHARMM36 <sup>46</sup>	256	8704	300	300	[47]
MacRog <sup>48</sup>	128	5120	300	500	[49]
Lipid14 <sup>50</sup>	72	2234	303	50	[51]
Slipids <sup>52</sup>	200	9000	310	500	[53]
ECC <sup>54</sup>	128	6400	300	300	[55]

<sup>a</sup>Number of POPC molecules.

<sup>b</sup>Number of water molecules.

<sup>c</sup>Simulation temperature.

<sup>d</sup>Trajectory length used for analysis.

<sup>e</sup>Reference for the openly available simulation files.

the NMRlipids Project to automatically recognise the atoms and bonds of interest for each trajectory.

After downloading the necessary files from Zenodo, we processed the trajectory with Gromacs `gmx trjconv` to make the molecules whole. We then calculated the  $S_{CH}$  (Eq. (3)) with the `OrderParameter.py` script that uses the MDanalysis<sup>76,77</sup> Python library. The C–H bond correlation functions  $g(\tau)$  (Eq. (1)) were calculated with Gromacs 5.1.4<sup>78</sup> `gmx rotacf` (note that in MD  $g_s = 1$  so that  $g = g_f$ ) after which the  $S_{CH}$  were used to normalize the  $g_f$  to obtain the reduced and normalized correlation function

$$g'_f(\tau) = \frac{g_f(\tau) - S_{CH}^2}{1 - S_{CH}^2}, \quad (7)$$

that is, the integrand in Eq. (4).

The effective correlation times  $\tau_e$  were then calculated by integrating  $g'_f(\tau)$  from  $\tau = 0$  until  $\tau = t_0$ . Here,  $t_0$  is the first time point at which  $g'_f$  reached zero:  $t_0 = \min\{t \mid g'_f(t) = 0\}$ . If  $g'_f$  did not reach zero within  $t_{\text{anal}}/2$ , the  $\tau_e$  was not determined, and we report only its upper and lower estimates.

To quantify the error on  $\tau_e$ , we first estimate

Table 2: Analyzed open-access MD trajectories of cholesterol-containing POPC bilayers at full hydration.

force field POPC/cholesterol	$c_{\text{chol}}^a$	$N_{\text{chol}}^b$	$N_l^c$	$N_w^d$	$T^e$ (K)	$t_{\text{anal}}^f$ (ns)	files <sup>g</sup>
Berger-POPC-07 <sup>44</sup>	0%	0	128	7290	298	50	[56]
/Höltje-CHOL-13 <sup>57,58</sup>	50%	64	64	10314	298	50	[59]
CHARMM36 <sup>46</sup>	0%	0	200	9000	310	500	[60]
/CHARMM36 <sup>61</sup>	50%	200	200	18000	310	500	[62]
MacRog <sup>48</sup>	0%	0	128	6400	310	500	[63]
/MacRog <sup>48</sup>	50%	64	64	6400	310	500	[63]
Slipids <sup>52</sup>	0%	0	200	9000	310	500	[53]
/Slipids <sup>64</sup>	50%	200	200	18000	310	500	[53]

<sup>a</sup>Bilayer cholesterol content (mol %).

<sup>b</sup>Number of cholesterol molecules.

<sup>c</sup>Number of POPC molecules.

<sup>d</sup>Number of water molecules.

<sup>e</sup>Simulation temperature.

<sup>f</sup>Trajectory length used for analysis.

<sup>g</sup>Reference for the openly available simulation files.

Table 3: Analyzed open-access MD trajectories of PC lipid bilayers under varying hydration level.

force field	lipid	$n_{w/l}^a$	$N_l^b$	$N_w^c$	$T^d$ (K)	$t_{\text{anal}}^e$ (ns)	files <sup>f</sup>
Berger-POPC-07 <sup>44</sup>	POPC	57	128	7290	298	50	[56]
	POPC	7	128	896	298	60	[65]
	POPC	40	256	10240	300	300	[45]
Berger-DLPC-13 <sup>66</sup>	DLPC <sup>g</sup>	24	72	1728	300	80	[67]
	DLPC <sup>g</sup>	16	72	1152	300	80	[68]
	DLPC <sup>g</sup>	12	72	864	300	80	[69]
	DLPC <sup>g</sup>	4	72	288	300	80	[70]
CHARMM36 <sup>46</sup>	POPC	40	128	5120	303	140	[71]
	POPC	34	128	5120	300	500	[49]
	POPC	31	72	2232	303	20	[72]
	POPC	15	72	1080	303	20	[73]
	POPC	7	72	504	303	20	[74]
MacRog <sup>48</sup>	POPC	50	288	14400	310	40	[75]
	POPC	25	288	7200	310	50	[75]
	POPC	15	288	4320	310	50	[75]
	POPC	10	288	2880	310	50	[75]
	POPC	5	288	1440	310	50	[75]

<sup>a</sup>Water/lipid molar ratio.

<sup>b</sup>Number of lipid molecules.

<sup>c</sup>Number of water molecules.

<sup>d</sup>Simulation temperature.

<sup>e</sup>Trajectory length used for analysis.

<sup>f</sup>Reference for the openly available simulation files.

<sup>g</sup>1,2-dilauroyl-sn-glycero-3-phosphocholine.

the error on  $g'_f(\tau)$ , where we account for two sources of uncertainty:  $g_f(\tau)$  and  $S_{\text{CH}}^2$ . Performing linear error propagation on Eq. (7) gives

$$\Delta g'_f(\tau) = \left| \frac{1}{1 - S_{\text{CH}}^2} \right| \Delta g_f(\tau) + \left| \frac{2(g_f(\tau) - 1) S_{\text{CH}}}{(1 - S_{\text{CH}}^2)^2} \right| \Delta S_{\text{CH}}. \quad (8)$$

Here the  $\Delta S_{\text{CH}}$  was determined as the standard error of the mean of the  $S_{\text{CH}}$  over the  $N_l$  individual lipids in the system.<sup>32</sup> Similarly, we quantified the error on  $g_f(\tau)$  by first determining the correlation function  $g_f^m(\tau)$  for each individual lipid  $m$  over the whole trajectory, and then obtaining the error estimate  $\Delta g_f(\tau)$  as the standard error of the mean over the  $N_l$  lipids. Importantly, this gives an uncertainty estimate for  $g_f(\tau)$  at each time point  $\tau$ .

To obtain the lower bound on  $\tau_e$ , we integrate the function  $g'_f(\tau) - \Delta g'_f(\tau)$  over time from  $\tau = 0$  until  $\tau = t_l$ . Here

$$t_l = \min \left\{ \{t \mid g'_f(t) - \Delta g'_f(t) = 0\}, \frac{t_{\text{anal}}}{2} \right\}. \quad (9)$$

That is,  $t_l$  equals the first time point at which the lower error estimate of  $g'_f$  reached zero; or  $t_l = t_{\text{anal}}/2$ , if zero was not reached before that point.

To obtain the upper error estimate on  $\tau_e$ , we first integrate the function  $g'_f(\tau) + \Delta g'_f(\tau)$  over time from  $\tau = 0$  until  $t_u = \min \{t_0, t_{\text{anal}}/2\}$ . Note, however, that this is not yet sufficient, because there could be slow processes that our simulation was not able to see. Although these would contribute to  $\tau_e$  with a low weight, their contribution over long times could still add up to a sizable effect on  $\tau_e$ . That said, it is feasible to assume (see Fig. 1A) that there are no longer-time contributions to  $g_f$  than something that decays with a time constant of  $10^{-6}$  s. We use this as our worst case estimate to assess the upper bound for  $\tau_e$ , that is, we assume that all the decay of  $g_f$  from the time point  $t_u$  onwards comes solely from this hypothetical slowest process that decays with a time constant of  $10^{-6}$  s. The additional contribution to the upper bound

for  $\tau_e$  then reads

$$(g'_f(t_u) + \Delta g'_f(t_u)) \times \underbrace{\int_{t_u}^{10^{-6} \text{ s}} \exp\left(-\frac{\tau - t_u}{10^{-6} \text{ s}}\right) d\tau}_{= (1 - \exp(-\frac{t_u - 10^{-6} \text{ s}}{10^{-6} \text{ s}})) 10^{-6} \text{ s}}. \quad (10)$$

The  $R_1$  rates were calculated using Eq. (5). The spectral density  $j(\omega)$  was obtained from the normalized correlation function  $g'_f$  by fitting it with a sum of 61 exponentials

$$g'_f(\tau) \approx \sum_{i=1}^{61} \alpha_i e^{-\tau/\tau_i}, \quad (11)$$

with logarithmically spaced time-scales  $\tau_i$  ranging from 1 ps to 1  $\mu$ s, and then calculating the spectral density of this fit based on the Fourier transformation<sup>41</sup>

$$j(\omega) = 2(1 - S_{\text{CH}}) \sum_{i=1}^{61} \alpha_i \frac{\tau_i}{1 + \omega\tau_i}. \quad (12)$$

The  $R_1$  rate of a given C–H pair was first calculated separately for each lipid  $m$  (using Eq. (5) with  $N_H = 1$ , and  $j^m(\omega)$  obtained for the normalized correlation function  $g'_f{}^m$ ). The resulting  $N_1$  measurements per C–H pair were then assumed independent: Their mean gave the  $R_1$  rate of the C–H pair, and standard error of the mean its uncertainty. The total  $R_1$  rate of a given carbon was obtained as a sum of the  $R_1$  rates of its C–H pairs. When several carbons contribute to a single experimental  $R_1$  rate due to the overlapping peaks (for example in C2 carbon in the acyl chains and the  $\gamma$  carbons), the  $R_1$  from simulations was obtained as an average over carbons with overlapping peaks. The segment-wise error estimates were obtained by standard error propagation, starting from the uncertainties of the  $R_1$  rates of the C–H pairs.

To gain some qualitative insight on the time scales at which the main contributions to the  $R_1$  rates arise, we also calculated 'cumulative'  $R_1$  rates,  $R_1(\tau)$ , which contained those terms of the sum in Eq. (12) for which  $\tau_i < \tau$ . Note that here the  $g'_f$  averaged over lipids was used; therefore, the 'cumulative'  $R_1(\tau \rightarrow \infty)$  does not nec-

essarily have exactly the same numerical value as the actual  $R_1$ .

Finally, we note that the fit of Eq. (11) provides an alternative to estimating  $\tau_e$ , because

$$\tau_e = \int_0^\infty g'_f(\tau) d\tau \approx \sum_i \alpha_i \tau_i. \quad (13)$$

When the simulation trajectory is not long enough for the correlation function to reach the plateau, integrating  $g'_f$  gives a lower bound estimate for  $\tau_e$ , while the sum of Eq. (13) includes also (some) contribution from the longer-time components via the fitting process. However, in practice the fit is often highly unreliable in depicting the long tails of the correlation function, and thus we chose to quantify  $\tau_e$  using the area under  $g'_f$ , and estimate its uncertainty as detailed above.

### 3 Results and Discussion

Using open-access MD simulation trajectories, we benchmark phospholipid conformational dynamics in six MD force fields. We start with pure POPC bilayers in their liquid crystalline fully hydrated state (see Table 1 for simulation details and Fig. 2 for the data), and then proceed to check the changes in dynamics when cholesterol is added to the bilayer (Table 2 and Fig. 4) and when the hydration level is reduced (Table 3 and Fig. 5). Our yardsticks are the effective correlations times  $\tau_e$  (Eq. (4)) and the  $R_1$  rates (Eq. (5)) measured at 125 MHz  $^{13}\text{C}$  (500 MHz  $^1\text{H}$ ) Larmor frequency; an MD model with correct rotational dynamics in a window around  $\sim 1$  ns will match the experimental  $R_1$  rates, whereas the  $\tau_e$  reflect all the sub- $\mu$ s time scales (Fig. 1).

#### Pure POPC at full hydration: Slipids and CHARMM36 reproduce $\tau_e$ excellently.

The top panels of Fig. 2 compare the effective correlation times  $\tau_e$  obtained for fully hydrated POPC bilayers in experiments (black) and in six different MD force fields (color). We see

that—as implied by the discussion leading to Eq. (10)—sub- $\mu$ s MD simulations typically lead to asymmetric error bars on  $\tau_e$ ; if these open-access trajectories were extended, the  $\tau_e$  values would more likely increase than decrease. Qualitatively, every force field captures the general shape of the  $\tau_e$  profile: Dynamics slows down towards the glycerol backbone in both the headgroup and the tails.

Quantitatively, most MD simulations tend to produce too slow dynamics in the glycerol region (Fig. 2). This is consistent with previous results for the Berger model,<sup>41</sup> and with the insufficient conformational sampling of glycerol backbone torsions observed in 500-ns-long CHARMMc32b2<sup>79,80</sup> simulations of a PC lipid.<sup>81</sup>

The best overall  $\tau_e$ -performance is seen in Slipids and in particular CHARMM36 (Fig. 2). This is in line with CHARMM36 reproducing the most realistic conformational ensembles for the headgroup and glycerol backbone among the MD simulation force fields benchmarked here.<sup>32,34</sup> Indeed, it is important to keep in mind that the conformational ensembles greatly differ between force fields and are not exactly correct in any of them.<sup>32,34</sup> Consequently, the calculated  $\tau_e$  times and  $R_1$  rates depict the dynamics of sampling a somewhat different and incorrect phase space for each model. To this end, we try to avoid overly detailed discussion on the models and rather concentrate on common and qualitative trends. That said, there are a few carbon segments in the data for which the experimental order parameters,  $R_1$ , and  $\tau_e$  are all (almost) reproduced by simulations, suggesting that the conformational ensemble and dynamics is correctly captured by MD in these cases. For example, Slipids performs well at the  $\beta$  and  $\alpha$ , and CHARMM36 at the  $g_3$ ,  $g_2$ , and C2 segments. These are, however, exceptions.

### **An excellent $\tau_e$ may be accompanied by a poor $R_1$ , or *vice versa*.**

The lower panels of Fig. 2 compare the experimental and simulated  $R_1$  rates under the same conditions that were used for the  $\tau_e$  above. Notably, there are several instances where the

$R_1$  comparison distinctly differs from what was seen for  $\tau_e$ .

There are cases where a matching  $R_1$  is accompanied by a larger-than-experimental  $\tau_e$ . MacRog for the  $\beta$ ,  $\alpha$ , and  $g_1$  segments provides a prominent example of this. Such a combination suggests that MD has the correct relative weight of 1-ns-scale dynamics, but has too slow long-time dynamics.

There are also cases where  $\tau_e$  matches experiments, but  $R_1$  does not, such as the  $\beta$  and  $\alpha$  segments in CHARMM36. Therein a cancellation of errors occurs in  $\tau_e$ : The overestimation of the relative weight of 1-ns-scale dynamics is compensated by wrong dynamics at the other time scales. As CHARMM36 overall performs rather well for C–H bond order parameters,  $R_1$ , and  $\tau_e$ , we proceed to study this shortcoming on the headgroup  $R_1$  rates in some more detail.

### **Conformational dynamics of PC headgroup segments in MD.**

Figure 3A zooms in on the headgroup ( $\gamma$ ,  $\beta$ ,  $\alpha$ ) segments, whose  $\tau_e$  were not clearly visible on the scale of Fig. 2. We see that for  $\gamma$ , no force field provides both  $\tau_e$  and  $R_1$ , but Slipids comes closest. For  $\beta$  and  $\alpha$ , Slipids captures both measurables near perfectly. In other words, among the benchmarked force fields Slipids gives the most realistic description of the conformational dynamics in the headgroup region. CHARMM36, e.g., overestimates ( $R_1$ ) the relative weight of timescales around  $\sim 1$  ns.

To investigate closer how the differences between force fields arise, Fig. 3B shows the ‘cumulative’  $R_1(\tau)$ , where the ranges of steepest increase indicate time scales that most strongly contribute to  $R_1$  rates.

For the  $\gamma$  segment, Fig. 3B shows that for models that overestimate the  $R_1$  rate (MacRog, CHARMM36, and Slipids, see Fig. 3A) the major contribution to  $R_1$  arises at  $\tau > 50$  ps, whereas for models that underestimate  $R_1$  (Lipid14 and ECC) the major contribution comes from  $\tau < 50$  ps. This also manifests in the distribution of fitting weights ( $\alpha_i$  in Eq. (11)) in Fig. 3C: The later non-zero weights occur, the larger is the resulting  $R_1$  of  $\gamma$ .

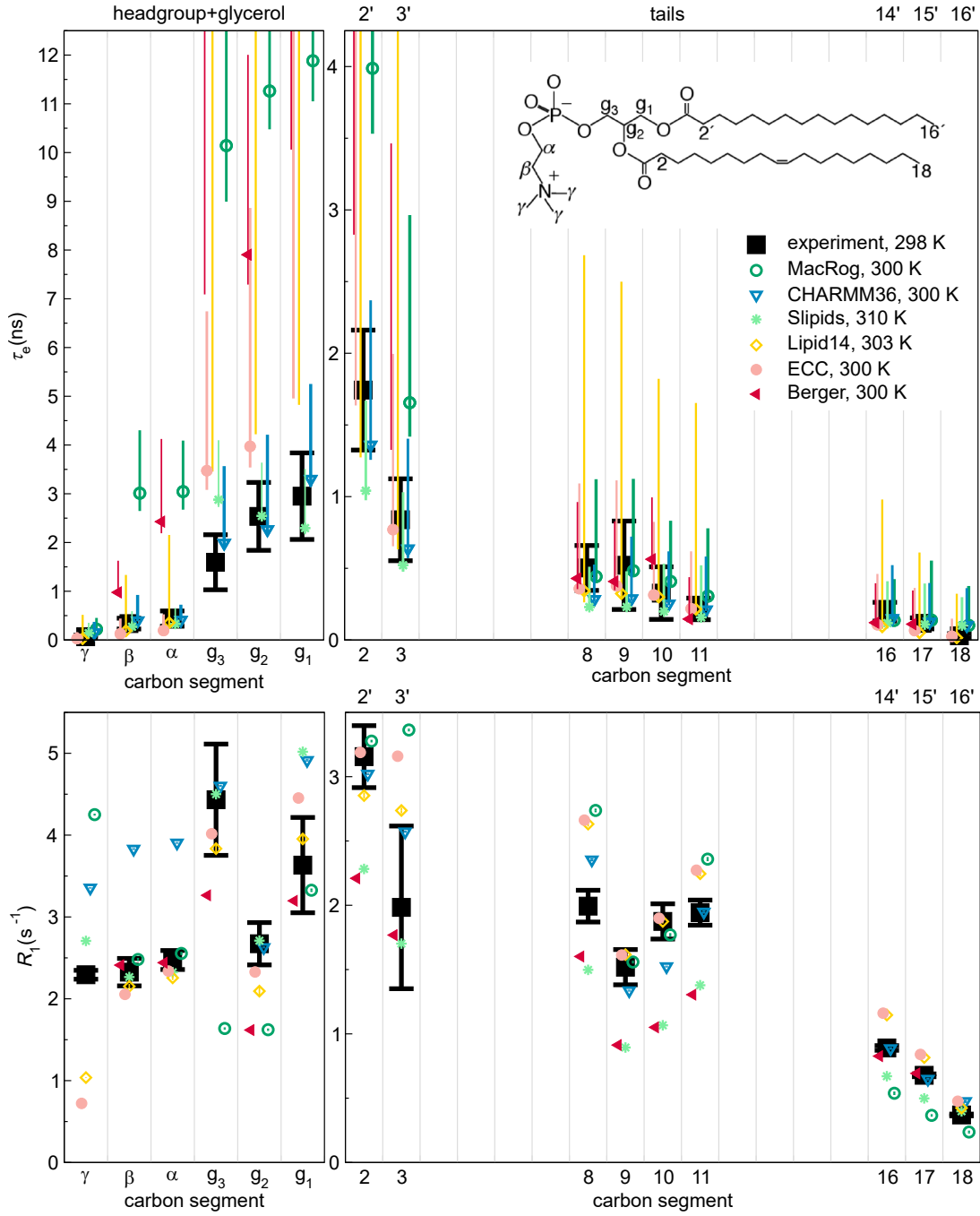


Figure 2: Effective correlation times ( $\tau_e$ , top) and  $R_1$  rates (bottom) in experiments<sup>39</sup> (black) and MD simulations (colored) of POPC bilayers in  $L_\alpha$  phase under full hydration. Inset shows the POPC chemical structure and carbon segment labeling. Each plotted value contains contributions from all the hydrogens within its carbon segment; the data for segments 8–11 are only from the sn-2 (oleoyl) chain, whereas the (experimentally non-resolved) contributions of both tails are included for segments 2–3 (2′–3′ in the sn-1 chain) and 16–18 (14′–16′). Simulation results are only shown for the segments for which experimental data was available. For  $\tau_e$ , a simulation data point indicates the average over C–H bonds; however, if  $\tau_e$  could not be determined for all bonds, only the error bar (extending from the mean of the lower to the mean of the upper error estimates) is shown. The Berger data for segments  $\gamma$ , C18, and C16′ are left out, as the protonation algorithm used to construct the hydrogens post-simulation in united atom models does not preserve the methyl C–H bond dynamics. Table 1 provides further simulation details, while information on the experiments is available at Ref. 39.



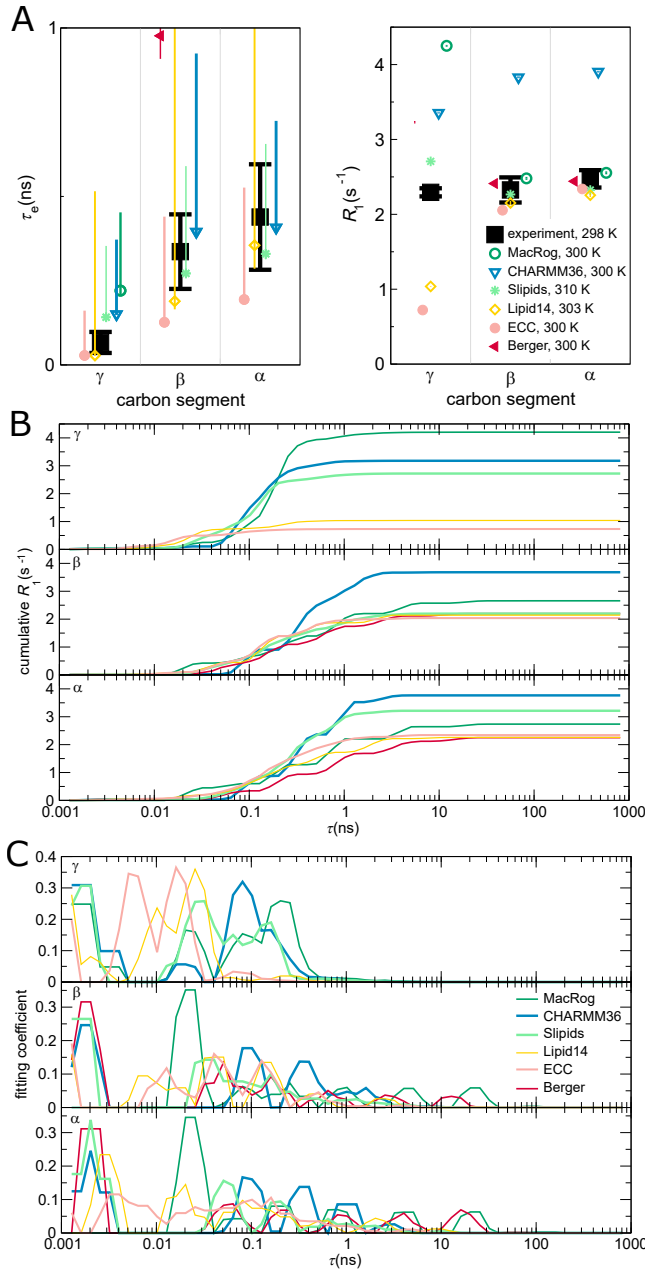


Figure 3: Contributions to the dynamics of the headgroup segments. (A) Zoom on the headgroup  $\tau_e$  (left panel) and  $R_1$  (right). (B) ‘Cumulative’  $R_1(\tau)$  of the  $\gamma$  (top panel),  $\beta$  (middle), and  $\alpha$  (bottom) segments.  $R_1(\tau)$  is obtained, as detailed in Methods, by including in the sum of Eq. (12) only terms with  $\tau_i < \tau$ . Consequently, at  $\tau \rightarrow \infty$  the  $R_1(\tau)$  approaches the actual  $R_1$ . (C) Prefactor weights  $\alpha_i$  from Eq. (11) of  $\gamma$  (top),  $\beta$  (middle), and  $\alpha$  (bottom). Note that panels B and C show a sliding average over 3 neighboring data points.

For the  $\beta$  and  $\alpha$  segments, Fig. 3B shows that the main contribution to  $R_1$  rates arises

from processes between 100 ps and 1 ns. CHARMM36 has the largest relative weights of all models in this window (Fig. 3C), which explains its overestimation of  $R_1$  of  $\beta$  and  $\alpha$ . All the other models have  $R_1$  rates close to experiments, but only Slipids simultaneously gives also the  $\tau_e$  correctly. Notably, Slipids has its largest weights at  $\tau < 100$  ps. Indeed, the considerable weights at short ( $< 10$  ps) time scales in all models except MacRog and at long ( $> 10$  ns) time scales in MacRog and Berger hardly manifest in  $R_1$ . However, the latter contribute heavily to  $\tau_e$ , which is thus considerably overestimated by MacRog and Berger (Fig. 2).

It would be highly interesting to identify the origins of the observed artificial timescales, particularly for the 0.1–1 ns window over-presented in CHARMM36, and propose how to correct those in the simulation models. However, the connection between the fitted correlation times and the correlation times of distinct motional processes, such as dihedral rotations and lipid wobbling, turns out to be highly non-trivial; we thus refrain from further analysis here.

## Effect of cholesterol.

An essential component in cell membranes, cholesterol has various biological functions. It is well known to order the acyl chains in lipid bilayers, but its effect on the headgroup is more controversial.<sup>58,82</sup> For example, it has been proposed that lipid headgroups reorganize to shield cholesterol from water.<sup>82</sup> However, while acyl chains do substantially order, NMR experiments show no significant conformational changes in the headgroup upon addition of even 50% of cholesterol—which suggests that the tail and head regions behave essentially independently.<sup>32,58</sup> In principle, the headgroups could shield cholesterol from water even without changing their conformational ensemble: By reorienting only laterally on top of the cholesterol. In this case, one would expect the rotational dynamics of headgroup segments to change when cholesterol is added.

Top panels of Fig. 4A depict the experimental effective correlation times  $\tau_e$  in pure POPC bilayers and in bilayers containing 50% chole-

terol. The  $\tau_e$  at the glycerol backbone slow down markedly when cholesterol is added. Tail segment dynamics slows down too, most notably close to the glycerol backbone. In stark contrast,  $\tau_e$  of the headgroup segments ( $\gamma$ ,  $\beta$ ,  $\alpha$ ) remain unaffected. Furthermore, cholesterol induces no measurable change in the headgroup  $\beta$  and  $\alpha$  segment dynamics at short ( $\sim 1$  ns) time scales, as demonstrated by the experimental  $R_1$  rates (Fig. 4A, bottom panels). That said, there is a small but measurable impact on  $R_1$  at  $\gamma$ . In summary, these experimental findings support the idea<sup>39</sup> that the acyl chains and the headgroup can respond almost independently to changes in conditions and composition.

All four benchmarked force fields (Fig. 4B) qualitatively reproduce the experimental increase in  $\tau_e$ : Slipids and CHARMM36 give rather decent magnitude estimates, while MacRog grossly overestimates the slowdown of glycerol, C2, and C3 segments. Notably, MacRog appears to predict slowdown also for the headgroup ( $\beta$  and  $\alpha$ ), for which experiments detect no change. Note that while CHARMM36 correctly shows no change in  $\tau_e$  of the  $\gamma$ ,  $\beta$ , and  $\alpha$  segments, it does predict an erroneous  $\Delta R_1$  for all three, indicating some inaccuracies in the headgroup rotational dynamics. Such inaccuracies might be reflected in the recent findings<sup>83</sup> (obtained using CHARMM36) that the headgroups of PCs neighboring (within 6.6 Å) a lone cholesterol spend more time on top of the said cholesterol than elsewhere. Interestingly, the tail  $\Delta R_1$  seem to be qualitatively reproduced by all three all-atom force fields, whereas Berger fails to capture the trend at the oleoyl double bond. All these findings are in line with the general picture obtained from C–H bond order parameters:<sup>38</sup> MD simulations capture the changes in acyl chain region rather well, but changes in and near the glycerol backbone region can be overestimated. Of the benchmarked force fields, CHARMM36 appears most realistic in reproducing the effects of cholesterol on the glycerol backbone—and Slipids on the PC headgroup—conformational dynamics.

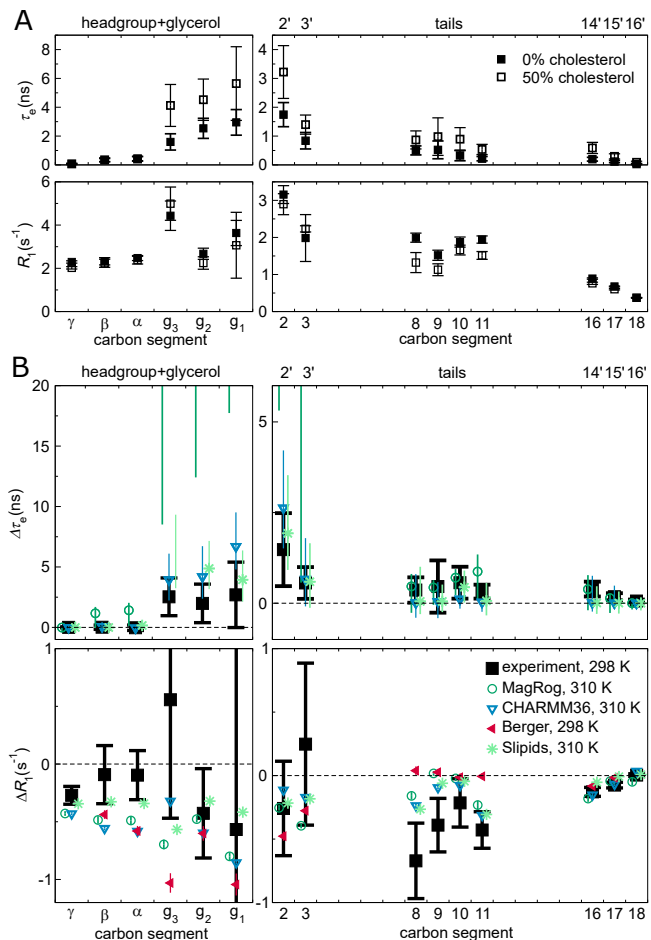


Figure 4: Effect of cholesterol on POPC conformational dynamics. (A) Experimental effective correlation times  $\tau_e$  (top panels) and  $R_1$  rates (bottom) in 100/0 and 50/50 POPC/cholesterol bilayers at full hydration, see Ref. 39 for further details. (B) The change in  $\tau_e$  ( $\Delta\tau_e$ , top panels) and  $R_1$  ( $\Delta R_1$ , bottom), in NMR (black) and MD (color), when bilayer composition changes from pure POPC to 50% cholesterol. Error estimates for the simulated  $\Delta\tau_e$  are the maximal possible based on the errors at 0% and 50% cholesterol; for other data regular error propagation is used. The Berger  $\Delta\tau_e$  is not shown, because the available open-access trajectories were too short to determine meaningful error estimates. Table 2 provides further simulation details; for segment labeling, see Fig. 2.

## Effect of drying.

Understanding the impact of dehydration on the structure and dynamics of lipid bilayers is of considerable biological interest. Dehydrated states are found, e.g., in skin tissue. Most

prominently, the process of membrane fusion is always preceded by removal of water between the approaching surfaces, and thus the dehydration-imposed changes can considerably affect fusion characteristics, such as its rate.

Figure 5A shows how a mild dehydration affects C-H bond dynamics in the PC headgroup and glycerol backbone; the plot compares the experimental effective correlation times  $\tau_e$  measured for POPC at full hydration and for DMPC (1,2-dimyristoyl-sn-glycero-3-phosphocholine) at 13 waters per lipid. The  $\tau_e$  are the same within experimental accuracy, which suggests two conclusions. Firstly, the headgroup ( $\gamma$ ,  $\beta$ ,  $\alpha$ )  $\tau_e$  are rather insensitive to the chemical identities of the tails. This is analogous to what was seen experimentally when adding cholesterol (Fig. 4A): Structural changes in the tail and glycerol regions do not (need to) affect the headgroup dynamics. Secondly, a mild dehydration does not alter the  $\tau_e$  in the headgroup and glycerol regions.

Figure 5B shows the effects of dehydration in three MD models. Combination of the unrealistically slow dynamics, especially in the glycerol backbone (Fig. 2), and the relatively short lengths of the available open-access trajectories (Table 3) led to large uncertainty estimates; thus we only point out qualitative trends here. For all headgroup and glycerol segments, the simulated  $\tau_e$  indicate slowdown upon dehydration. This is manifested in the increase in the magnitude of the error estimate (cf. the Berger data for  $\beta$  and  $\alpha$ ) as well as in the increase of the lower limit of the error. For CHARMM36 the lower error estimates stay almost constant all the way until 7 w/l, whereas for Berger and MacRog they hint that a retardation of dynamics starts already between 15 and 10 w/l.

These simulational findings suggest that experiments reducing hydration levels below 10 w/l would also show an increase in  $\tau_e$ . This prediction is in line with the exponential slowdown of the headgroup conformational dynamics upon dehydration that was indicated by  $^2\text{H}$ -NMR  $R_1$  measurements of DOPC bilayers:  $R_1 \sim \exp(-n_{\text{w/l}}/4)$ .<sup>84</sup> The slowdown was attributed to the reduced effective volume available for the headgroup<sup>84</sup> as it tilts towards the

membrane upon dehydration; such tilt is observed via changes of the lipid headgroup order parameters,<sup>85</sup> and is qualitatively reproduced by all the simulation models.<sup>32</sup>

Figure 5C shows a collection of experimental  $^{13}\text{C}$ -NMR  $R_1$  rates for the headgroup segments at different water contents; in addition to the full hydration POPC data from Fig. 2, DMPC at 13 w/l,<sup>42</sup> and POPC at 20 and 5 w/l<sup>43</sup> are shown. Experimentally, an increasing trend with decreasing hydration is observed for all three segments, indicating changes of headgroup dynamics at short ( $\sim 1$  ns) time scales. Interestingly, only CHARMM36 captures this, whereas Berger and MacRog give decreasing  $R_1$  rates for  $\beta$  and  $\alpha$ .

The slowdown characteristics discussed here are of significance not only for computational studies of intermembrane interactions, such as fusion, but also when simulating a bilayer (stack) under low hydration: Slower dynamics require longer simulation times for equilibration, for reliably quantifying the properties of the bilayers, and for observing rare events.

## 4 Conclusions

Open access databanks of MD trajectories enables the creation new scientific information without running a single new simulation. Here, we demonstrated this by investigating the dynamics of a wide range of phosphatidylcholine molecular dynamics models using the existing trajectories from the NMRlipids databank.

We found that MD qualitatively captures the  $^{13}\text{C}$ -NMR effective correlation time ( $\tau_e$ ) profile of POPC—the slow glycerol backbone and the faster motions of the headgroup and tail regions—but most MD force fields are prone to too slow dynamics of the glycerol C-H bonds (Fig. 2). While no force field perfectly reproduces all the experimental data, CHARMM36 and Slipids have an overall impressive  $\tau_e$ . This is particularly true for CHARMM36, as it is also known to well represent the experimental conformational ensemble.<sup>32</sup> That said, we find that CHARMM36 struggles with the balance of dynamics in the headgroup region: The  $R_1$

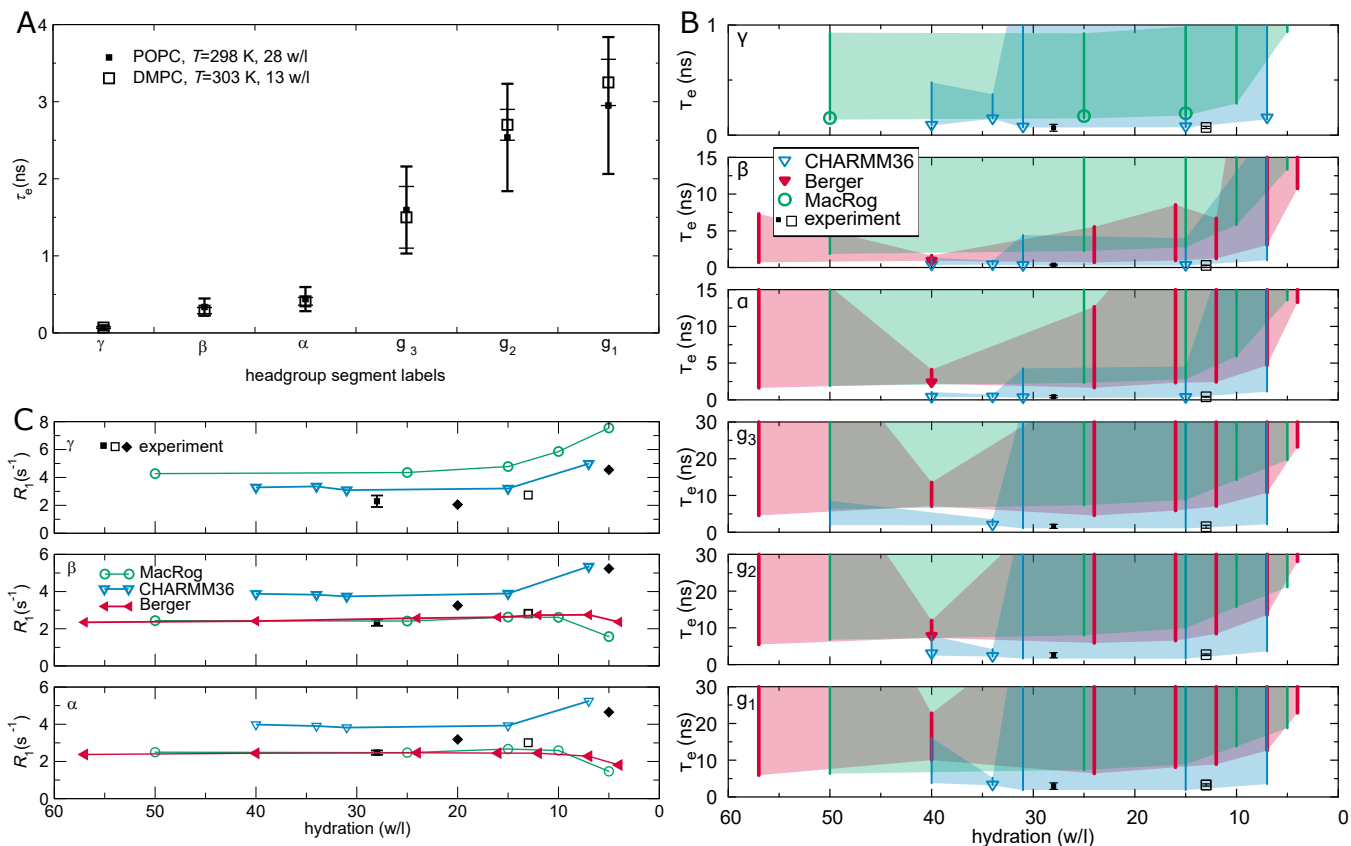


Figure 5: Effect of drying on PC headgroup and glycerol backbone conformational dynamics. (A) Experimental effective correlation times  $\tau_e$  for DMPC at low hydration (from Ref. 42) do not significantly differ from the  $\tau_e$  for POPC at full hydration (from Ref. 39). (B) Calculated  $\tau_e$  for POPC at decreasing hydration in three MD models. Symbols indicate the mean of segment hydrogens if  $\tau_e$  could be determined for all of them; otherwise, only the error bar (extending from the mean of the lower to the mean of the upper uncertainty estimates) is drawn. The area limited by the error bars shaded for visualization. Note that four Berger data points (4, 12, 16, and 24 w/l) are from DLPC. (C)  $^{13}\text{C}$ -NMR  $R_1$  rates (at  $\omega_C = 125$  MHz) of the PC headgroup segments in experiments and simulations: Experiments indicate an increasing trend upon dehydration. Experimental POPC data at 28 w/l is from Ref. 39 (■), POPC at 20 and 5 w/l from Ref. 43 (◆), and DMPC at 13 w/l from Ref. 42 (□). See Table 3 for simulation details.

rates, sensitive for  $\sim 1$ -ns processes, are too high for the  $\gamma$ ,  $\beta$ , and  $\alpha$  segments (Fig. 3).

In addition to standard conditions, we explored how the dynamics react to addition of cholesterol and removal of water. MD qualitatively captures the slow-down of conformational dynamics in the tail and glycerol regions when cholesterol is mixed into a POPC bilayer; however, some force fields erroneously predict changes also in the short-scale dynamics of the headgroup carbons (Fig. 4). Upon reducing the water content, MD exhibits slow-down of headgroup and backbone dynamics below  $\sim 10$  waters per lipid in qualitative agreement with ex-

perimental data. That said, only CHARMM36 qualitatively captures the experimentally detected increase of  $R_1$  rates upon dehydration.

By gathering a set of  $^{13}\text{C}$ -NMR data on the phosphatidylcholine dynamics and charting the typical features of the existing MD models against it, this study lays the foundation for further improvement of the force fields. While work is still needed in capturing even the correct conformations,<sup>32</sup> realistic dynamics will be an essential part of developing MD into a true computational microscope.

Importantly, this work demonstrates the potential of open data in achieving this at a re-

duced computational and labor cost. A pool of well indexed and documented data provides an ideal platform for automation, and thus has the potential to facilitate faster progress in pinpointing the typical failures of existing models, in identifying key differences in models describing chemical variations under the same molecule type (eg. different lipid headgroups), and developing better models through machine learning approaches.

## Acknowledgement

H.A gratefully acknowledges the support from Osk. Huttunen’s foundation, Finnish Academy of Science and Letters (Foundations’ Post Doc Pool), Instrumentarium Science Foundation, and the AvH Foundation.

## References

- (1) Crystallography: Protein Data Bank. *Nat. New Biol.* **1971**, *233*, 223.
- (2) wwPDB consortium, Protein Data Bank: the single global archive for 3D macromolecular structure data. *Nucleic Acids Res.* **2019**, *47*, D520–D528.
- (3) Jordan, E.; Carrico, C. DNA Database. *Science* **1982**, *218*, 108.
- (4) Sayers, E. W.; Cavanaugh, M.; Clark, K.; Ostell, J.; Pruitt, K. D.; Karsch-Mizrachi, I. GenBank. *Nucleic. Acids Res.* **2020**, *48*, D84–D86.
- (5) Levitt, M. Growth of novel protein structural data. *Proceedings of the National Academy of Sciences* **2007**, *104*, 3183–3188.
- (6) Brzezinski, D.; Dauter, Z.; Minor, W.; Jaskolski, M. On the evolution of the quality of macromolecular models in the PDB. *The FEBS Journal* **2020**, *287*, 2685–2698.
- (7) Harris, D. J. Can you bank on GenBank? *Trends in Ecology & Evolution* **2003**, *18*, 317–319.
- (8) Steinegger, M.; Salzberg, S. L. Terminating contamination: large-scale search identifies more than 2,000,000 contaminated entries in GenBank. *Genome Biology* **2020**, *21*, 115.
- (9) Rigden, D. J.; Fernández, X. M. The 27th annual Nucleic Acids Research database issue and molecular biology database collection. *Nucleic Acids Research* **2020**, *48*, D1–D8.
- (10) Simpkin, A. J.; Thomas, J. M. H.; Simkovic, F.; Keegan, R. M.; Rigden, D. J. Molecular replacement using structure predictions from databases. *Acta Crystallographica Section D Structural Biology* **2019**, *D75*, 1051–1062.
- (11) Leelananda, S. P.; Lindert, S. Using NMR Chemical Shifts and Cryo-EM Density Restraints in Iterative Rosetta-MD Protein Structure Refinement. *Journal of Chemical Information and Modeling* **2020**, *60*, 2522–2532.
- (12) Senior, A. W. et al. Improved protein structure prediction using potentials from deep learning. *Nature* **2020**, *577*, 706–710.
- (13) Huang, P.-S.; Boyken, S. E.; Baker, D. The coming of age of de novo protein design. *Nature* **2016**, *537*, 320.
- (14) Westbrook, J. D.; Burley, S. K. How Structural Biologists and the Protein Data Bank Contributed to Recent FDA New Drug Approvals. *Structure* **2019**, *27*, 211–217.
- (15) Martinez-Mayorga, K.; Madariaga-Mazon, A.; Medina-Franco, J.; Maggiora, G. The impact of chemoinformatics on drug discovery in the pharmaceutical industry. *Expert Opinion on Drug Discovery* **2020**, *15*, 293–306.
- (16) Senderowitz, H.; Tropsha, A. Materials Informatics. *J. Chem. Inf. Model.* **2018**, *58*, 2377–2379.

- (17) Wan, X.; Feng, W.; Wang, Y.; Wang, H.; Zhang, X.; Deng, C.; Yang, N. Materials Discovery and Properties Prediction in Thermal Transport via Materials Informatics: A Mini Review. *Nano Letters* **2019**, *19*, 3387–3395.
- (18) Perez-Riverol, Y.; Zorin, A.; Dass, G.; Vu, M.-T.; Xu, P.; Glont, M.; Vizcaíno, J. A.; Jarnuczak, A. F.; Petryszak, R.; Ping, P.; Hermjakob, H. Quantifying the impact of public omics data. *Nature Communications* **2019**, *10*.
- (19) Feng, Z.; Verdigué, N.; Costanzo, L. D.; Goodsell, D. S.; Westbrook, J. D.; Bursley, S. K.; Zardecki, C. Impact of the Protein Data Bank Across Scientific Disciplines. *Data Science Journal* **2020**, *19*, 25.
- (20) Feig, M.; Abdullah, M.; Johnsson, L.; Pettitt, B. M. Large scale distributed data repository: design of a molecular dynamics trajectory database. *Future Generation Computer Systems* **1999**, *16*, 101–110.
- (21) Tai, K.; Murdock, S.; Wu, B.; Ng, M. H.; Johnston, S.; Fangohr, H.; Cox, S. J.; Jeffreys, P.; Essex, J. W.; Sansom, M. S. BioSimGrid: towards a worldwide repository for biomolecular simulations. *Organic & Biomolecular Chemistry* **2004**, *2*, 3219–3221.
- (22) Silva, C. G.; Ostroptsyky, V.; Loureiro-Ferreira, N.; Berrar, D.; Swain, M.; Dubitzky, W.; Brito, R. M. M. P-found: The Protein Folding and Unfolding Simulation Repository. 2006 IEEE Symposium on Computational Intelligence and Bioinformatics and Computational Biology. 2006; pp 1–8.
- (23) Hildebrand, P. W.; Rose, A. S.; Tieermann, J. K. S. Bringing Molecular Dynamics Simulation Data into View. *Trends in Biochemical Sciences* **2019**, *44*, 902–913.
- (24) Abraham, M. et al. Sharing Data from Molecular Simulations. *Journal of Chemical Information and Modeling* **2019**, *59*, 4093–4099.
- (25) Abriata, L. A.; Lepore, R.; Dal Peraro, M. About the need to make computational models of biological macromolecules available and discoverable. *Bioinformatics* **2020**, *36*, 2952–2954.
- (26) Hospital, A.; Battistini, F.; Soliva, R.; Gelpí, J. L.; Orozco, M. Surviving the deluge of biosimulation data. *WIREs Computational Molecular Science* **2020**, *10*, e1449.
- (27) Hospital, A.; Andrio, P.; Cugnasco, C.; Codo, L.; Becerra, Y.; Dans, P. D.; Battistini, F.; Torres, J.; Goñi, R.; Orozco, M.; Gelpí, J. L. BIGNASim: a NoSQL database structure and analysis portal for nucleic acids simulation data. *Nucleic Acids Research* **2016**, *44*, D272–D278.
- (28) Bekker, G.-J.; Kawabata, T.; Kurisu, G. The Biological Structure Model Archive (BSM-Arc): an archive for in silico models and simulations. *Biophysical Reviews* **2020**, *12*, 371–375.
- (29) Mixcoha, E.; Rosende, R.; Garcia-Fandino, R.; Piñeiro, Á. Cyclo-lib: a database of computational molecular dynamics simulations of cyclodextrins. *Bioinformatics* **2016**, *32*, 3371–3373.
- (30) Rodríguez-Espigares, I. et al. GPCRmd uncovers the dynamics of the 3D-GPCRome. *bioRxiv* **2019**, 839597.
- (31) Miettinen, M. S.; NMRlipids Collaboration; Ollila, O. H. S. LDB: Lipid Data-bank from the NMRlipids Project. *Biophysical Journal* **2019**, *116*, 91a.
- (32) Botan, A. et al. Toward Atomistic Resolution Structure of Phosphatidylcholine Headgroup and Glycerol Backbone at Different Ambient Conditions. *The Journal of Physical Chemistry B* **2015**, *119*, 15075–15088, PMID: 26509669.

- (33) Catte, A.; Girych, M.; Javanainen, M.; Loison, C.; Melcr, J.; Miettinen, M. S.; Monticelli, L.; Määttä, J.; Oganessian, V. S.; Ollila, O. H. S.; Tynkkynen, J.; Vilov, S. Molecular electrometer and binding of cations to phospholipid bilayers. *Phys. Chem. Chem. Phys.* **2016**, *18*, 32560–32569.
- (34) Antila, H.; Buslaev, P.; Favela-Rosales, F.; Ferreira, T. M.; Gushchin, I.; Javanainen, M.; Kav, B.; Madsen, J. J.; Melcr, J.; Miettinen, M. S.; Määttä, J.; Nencini, R.; Ollila, O. H. S.; Piggot, T. J. Headgroup Structure and Cation Binding in Phosphatidylserine Lipid Bilayers. *J. Phys. Chem. B* **2019**, *123*, 9066–9079.
- (35) Robustelli, P.; Piana, S.; Shaw, D. E. Developing a molecular dynamics force field for both folded and disordered protein states. *Proc. Natl. Acad. Sci.* **2018**, *115*, E4758–E4766.
- (36) Henriques, J.; Arleth, L.; Lindorff-Larsen, K.; Skepö, M. On the Calculation of SAXS Profiles of Folded and Intrinsically Disordered Proteins from Computer Simulations. *J. Mol. Biol.* **2018**, *430*, 2521 – 2539.
- (37) Virtanen, S. I.; Kiirikki, A. M.; Mikula, K. M.; Iwai, H.; Ollila, O. H. S. Heterogeneous dynamics in partially disordered proteins. *Phys. Chem. Chem. Phys.* **2020**, –.
- (38) Ollila, S.; Pabst, G. Atomistic resolution structure and dynamics of lipid bilayers in simulations and experiments. *BBA - Biomembranes* **2016**, *1858*, 2512–2528.
- (39) Antila, H. S.; Wurl, A.; Ollila, O. H. S.; Miettinen, M. S.; Ferreira, T. M. Quasi-uncoupled rotational diffusion of phospholipid headgroups from the main molecular frame. *arXiv preprint* **2020**, arXiv:2009.06774v1.
- (40) Han, J.; Pluhackova, K.; Böckmann, R. A. The Multifaceted Role of SNARE Proteins in Membrane Fusion. *Frontiers in Physiology* **2017**, *8*, 5.
- (41) Ferreira, T. M.; Ollila, O. H. S.; Pigliapochi, R.; Dabkowska, A. P.; Topgaard, D. Model-free estimation of the effective correlation time for C–H bond reorientation in amphiphilic bilayers:  $^1\text{H}$ – $^{13}\text{C}$  solid-state NMR and MD simulations. *The Journal of Chemical Physics* **2015**, *142*, 044905.
- (42) Pham, Q. D.; Topgaard, D.; Sparr, E. Cyclic and Linear Monoterpenes in Phospholipid Membranes: Phase Behavior, Bilayer Structure, and Molecular Dynamics. *Langmuir* **2015**, *31*, 11067–11077, PMID: 26375869.
- (43) Volke, F.; Pampel, A. Membrane Hydration and Structure on a Subnanometer Scale as Seen by High Resolution Solid State Nuclear Magnetic Resonance: POPC and POPC/ $\text{C}_{12}\text{EO}_4$  Model Membranes. *Biophys. J.* **1995**, *68*, 1960–1965.
- (44) Ollila, S.; Hyvönen, M. T.; Vattulainen, I. Polyunsaturation in Lipid Membranes: Dynamic Properties and Lateral Pressure Profiles. *J. Phys. Chem. B* **2007**, *111*, 3139–3150.
- (45) Bacle, A.; Fuchs, P. F. Berger pure POPC MD simulation (300 K - 300ns - 1 bar). 2018; {<https://doi.org/10.5281/zenodo.1402417>}.
- (46) Klauda, J. B.; Venable, R. M.; Freites, J. A.; O'Connor, J. W.; Tobias, D. J.; Mondragon-Ramirez, C.; Vorobyov, I.; Jr, A. D. M.; Pastor, R. W. Update of the CHARMM All-Atom Additive Force Field for Lipids: Validation on Six Lipid Types. *J. Phys. Chem. B* **2010**, *114*, 7830–7843.
- (47) Papadopoulos, C.; Fuchs, P. F. CHARMM36 pure POPC MD simulation (300 K - 300ns - 1 bar). 2018; <http://dx.doi.org/10.5281/zenodo.1306800>, DOI: 10.5281/zenodo.1306800.



- (48) Kulig, W.; Jurkiewicz, P.; Olżyńska, A.; Tynkkynen, J.; Javanainen, M.; Manna, M.; Rog, T.; Hof, M.; Vattulainen, I.; Jungwirth, P. Experimental determination and computational interpretation of biophysical properties of lipid bilayers enriched by cholesterol hemisuccinate. *Biochim. Biophys. Acta* **2015**, *1848*, 422 – 432.
- (49) Milan Rodriguez, P.; Fuchs, P. F. MacRog pure POPC MD simulation (300 K - 500ns - 1 bar). **2020**,
- (50) Dickson, C. J.; Madej, B. D.; Skjevik, A. A.; Betz, R. M.; Teigen, K.; Gould, I. R.; Walker, R. C. Lipid14: The Amber Lipid Force Field. *J. Chem. Theory Comput.* **2014**, *10*, 865–879.
- (51) Ollila, O. H. S.; Retegan, M. MD simulation trajectory and related files for POPC bilayer (Lipid14, Gromacs 4.5). 2014; DOI: 10.5281/zenodo.12767.
- (52) Jämbeck, J. P. M.; Lyubartsev, A. P. An Extension and Further Validation of an All-Atomistic Force Field for Biological Membranes. *J. Chem. Theory Comput.* **2012**, *8*, 2938–2948.
- (53) Javanainen, M. POPC with 0, 10, 20, and 30 mol-Slipids force field. 2016; <http://dx.doi.org/10.5281/zenodo.3243328>.
- (54) Melcr, J.; Martinez-Seara, H.; Nencini, R.; Kolafa, J.; Jungwirth, P.; Ollila, O. H. S. Accurate Binding of Sodium and Calcium to a POPC Bilayer by Effective Inclusion of Electronic Polarization. *The Journal of Physical Chemistry B* **2018**, *122*, 4546–4557.
- (55) Melcr, J. Simulations of POPC lipid bilayer in water solution at various NaCl, KCl and CaCl<sub>2</sub> concentrations using ECC-POPC force field. **2019**,
- (56) Ollila, O. H. S.; Ferreira, T.; Topgaard, D. MD simulation trajectory and related files for POPC bilayer (Berger model delivered by Tieleman, Gromacs 4.5). 2014; <http://dx.doi.org/10.5281/zenodo.13279>.
- (57) Hölte, M.; Förster, T.; Brandt, B.; Engels, T.; von Rybinski, W.; Hölte, H.-D. Molecular dynamics simulations of stratum corneum lipid models: fatty acids and cholesterol. *Biochim. Biophys. Acta* **2001**, *1511*, 156 – 167.
- (58) Ferreira, T. M.; Coreta-Gomes, F.; Ollila, O. H. S.; Moreno, M. J.; Vaz, W. L. C.; Topgaard, D. Cholesterol and POPC segmental order parameters in lipid membranes: solid state <sup>1</sup>H–<sup>13</sup>C NMR and MD simulation studies. *Phys. Chem. Chem. Phys.* **2013**, *15*, 1976–1989.
- (59) Ollila, O. H. S. MD simulation trajectory and related files for POPC/cholesterol (50 molmodified Hölte, Gromacs 4.5). **2014**,
- (60) Javanainen, M. POPC with 0, 10, 20, and 30 mol-Charmm36 force field. 2016; <https://doi.org/10.5281/zenodo.3237420>, DOI: 10.5281/zenodo.3237420.
- (61) Lim, J. B.; Rogaski, B.; Klauda, J. B. Update of the Cholesterol Force Field Parameters in CHARMM. *J. Phys. Chem. B* **2012**, *116*, 203–210.
- (62) Javanainen, M. POPC with 40 and 50 mol-force field. 2016; <https://doi.org/10.5281/zenodo.3238157>, DOI: 10.5281/zenodo.3238157.
- (63) Javanainen, M.; Kulig, W. POPC/Cholesterol @ 310K. 0, 10, 40, 50 and 60 mol-cholesterol. Model by Maciejewski and Rog. **2015**,
- (64) Jämbeck, J. P. M.; Lyubartsev, A. P. Another Piece of the Membrane Puzzle: Extending Slipids Further. *Journal of Chemical Theory and Computation* **2013**, *9*, 774–784, PMID: 26589070.
- (65) Ollila, O. H. S. MD simulation trajectory and related files for POPC bilayer in low hydration (Berger model delivered by Tieleman, Gromacs 4.5). **2015**,



- (66) Kanduc, M.; Schneck, E.; Netz, R. R. Hydration Interaction between Phospholipid Membranes: Insight into Different Measurement Ensembles from Atomistic Molecular Dynamics Simulations. *Langmuir* **2013**, *29*, 9126–9137.
- (67) Kanduc, M. MD trajectory for DLPC bilayer (Berger, Gromacs 4.5.4), nw=24 w/l. 2015; DOI: 10.5281/zenodo.16289.
- (68) Kanduc, M. MD trajectory for DLPC bilayer (Berger, Gromacs 4.5.4), nw=16 w/l. 2015; DOI: 10.5281/zenodo.16292.
- (69) Kanduc, M. MD trajectory for DLPC bilayer (Berger, Gromacs 4.5.4), nw=12 w/l. 2015; DOI: 10.5281/zenodo.16293.
- (70) Kanduc, M. MD trajectory for DLPC bilayer (Berger, Gromacs 4.5.4), nw=4 w/l. 2015; DOI: 10.5281/zenodo.16295.
- (71) Santuz, H. MD simulation trajectory and related files for POPC bilayer (CHARMM36, Gromacs 4.5). 2015; <http://dx.doi.org/10.5281/zenodo.14066>, DOI: 10.5281/zenodo.14066.
- (72) Ollila, O. H. S.; Miettinen, M. MD simulation trajectory and related files for POPC bilayer (CHARMM36, Gromacs 4.5). 2015; <http://dx.doi.org/10.5281/zenodo.13944>, DOI: 10.5281/zenodo.13944.
- (73) Ollila, O. H. S.; Miettinen, M. MD simulation trajectory and related files for POPC bilayer in medium low hydration (CHARMM36, Gromacs 4.5). 2015; <http://dx.doi.org/10.5281/zenodo.13946>, DOI: 10.5281/zenodo.13946.
- (74) Ollila, O. H. S.; Miettinen, M. MD simulation trajectory and related files for POPC bilayer in low hydration (CHARMM36, Gromacs 4.5). 2015; <http://dx.doi.org/10.5281/zenodo.13945>, DOI: 10.5281/zenodo.13945.
- (75) Javanainen, M. POPC @ 310K, varying water-to-lipid ratio. Model by Maciejewski and Rog. 2014; <http://dx.doi.org/10.5281/zenodo.13498>, DOI: 10.5281/zenodo.13498.
- (76) Michaud-Agrawal, N.; Denning, E. J.; Woolf, T. B.; Beckstein, O. MDAnalysis: A toolkit for the analysis of molecular dynamics simulations. *Journal of Computational Chemistry* **2011**, *32*, 2319–2327.
- (77) Richard J. Gowers,; Max Linke,; Jonathan Barnoud,; Tyler J. E. Reddy,; Manuel N. Melo,; Sean L. Seyler,; Jan Domański,; David L. Dotson,; Sébastien Buchoux,; Ian M. Kenney,; Oliver Beckstein, MDAnalysis: A Python Package for the Rapid Analysis of Molecular Dynamics Simulations. Proceedings of the 15th Python in Science Conference. 2016; pp 98 – 105.
- (78) Abraham, M. J.; Murtola, T.; Schulz, R.; Páll, S.; Smith, J. C.; Hess, B.; Lindahl, E. GROMACS: High performance molecular simulations through multi-level parallelism from laptops to supercomputers. *SoftwareX* **2015**, *1*, 19–25.
- (79) Schlenkrich, M.; Brickmann, J.; MacKerell, A. D.; Karplus, M. *Biological Membranes*; Springer, 1996; pp 31–81.
- (80) Feller, S. E.; MacKerell, A. D. An improved empirical potential energy function for molecular simulations of phospholipids. *The Journal of Physical Chemistry B* **2000**, *104*, 7510–7515.
- (81) Vogel, A.; Feller, S. E. Headgroup Conformations of Phospholipids from Molecular Dynamics Simulation: Sampling Challenges and Comparison to Experiment. *The Journal of Membrane Biology* **2012**, *245*, 23–28.
- (82) Huang, J.; Feigenson, G. W. A Microscopic Interaction Model of Maximum Solubility of Cholesterol in Lipid Bilayers. *Biophysical Journal* **1999**, *76*, 2142 – 2157.
- (83) Leeb, F.; Maibaum, L. Spatially Resolving the Condensing Effect of Cholesterol in

Lipid Bilayers. *Biophysical Journal* **2018**, *115*, 2179 – 2188.

- (84) Ulrich, A.; Watts, A. Molecular response of the lipid headgroup to bilayer hydration monitored by 2H-NMR. *Biophys. J.* **1994**, *66*, 1441 – 1449.
- (85) Bechinger, B.; Seelig, J. Conformational changes of the phosphatidylcholine headgroup due to membrane dehydration. A 2H-NMR study. *Chemistry and Physics of Lipids* **1991**, *58*, 1 – 5.

## Graphical TOC Entry

TOC here if needed